actuators

MDPI

Article

Design and Optimization of Asymmetrical Rotor Structure for Permanent Magnet Synchronous Motors

Jianjun Hu *, Xin Wang, Xing Zhang and Zutang Yao

State Key Laboratory of Mechanical Transmission for Advanced Equipment, Chongqing University, Chongqing 400044, China; youarebest1007@163.com (X.W.); zx0815fighting@163.com (X.Z.); yaozutang@cqu.edu.cn (Z.Y.)

* Correspondence: hujianjun@cqu.edu.cn

Abstract

Permanent magnet synchronous motors (PMSMs) are widely employed in electric vehicles owing to their high efficiency, high power density, and wide speed regulation capability. However, electromagnetic vibration is aggravated by the non-sinusoidal air gap magnetic field distribution and cogging torque. To suppress vibration, this paper proposes an optimized asymmetric rotor design. Through sensitivity analysis of rotor parameters on motor performance, a high-precision Metamodel of Optimal Prognosis (MOP) is developed for the surrogate-based motor model. Subsequently, rotor parameters are comprehensively optimized using a genetic algorithm. The results demonstrate that, compared with the reference motor under identical operating conditions, the optimized motor maintains equivalent output torque while achieving significant reductions in vibration-related performance indicators: torque ripple is reduced by 17.9%, and cogging torque is reduced by 82.8%, the amplitude of the 48th-order electromagnetic force decreases from 2.60 N to 1.28 N (representing a 50.7% reduction), and the peak vibration response decreases from 109.7 dB to 107.2 dB. This study provides an effective design approach for electromagnetic vibration suppression in PMSMs.

Keywords: PMSM; electromagnetic vibration; cogging torque; rotor optimization; finite element analysis

1. Introduction

Permanent magnet synchronous motors (PMSMs) are widely employed in electric vehicles owing to their high power density, high efficiency, wide speed regulation capability, and excellent reliability [1]. With the rapid expansion of the new energy vehicle market, consumer demands have extended beyond power performance, energy economy, and safety to include driving comfort, low vibration, and minimal noise, which have become critical selection criteria. The vibration characteristics of PMSMs can generally be classified into two categories according to their excitation sources: mechanical vibration and electromagnetic vibration [2]. Mechanical vibration mainly originates from bearing defects, gear meshing, and rotor imbalance, whereas electromagnetic vibration is induced by electromagnetic force waves acting on the stator structure. In vehicle traction motors, high rotational speeds increase the excitation frequency range and the risk of resonance caused by electromagnetic and mechanical excitations. In particular, radial electromagnetic forces, high-order harmonic components, and cogging torque can excite stator deformation and housing vibration, thereby deteriorating the vibration and acoustic performance of PMSMs.

Academic Editor: Paolo Mercorelli

Received: 15 June 2026
Revised: 9 July 2026
Accepted: 14 July 2026
Published: 15 July 2026

Currently, electromagnetic vibration and noise in PMSMs are mainly mitigated through two approaches: control-oriented suppression and structural optimization design. Control-oriented suppression methods regulate electromagnetic excitations by dynamically adjusting current harmonics. Martin et al. [3] achieved an approximately 10 dB reduction in the total sound pressure level of a PMSM using flux harmonic injection. Le et al. [4] suppressed radial vibration by optimizing the frequency, amplitude, and phase of current harmonics. Ji et al. [5] employed a quasi-proportional resonant controller to compensate for specific harmonic currents and reduce low-frequency torque ripple in IPMSMs. Similarly, Wang et al. [6] combined low-frequency pulse voltage injection with an adaptive observer to attenuate electromagnetic force excitation caused by current harmonics; however, the achievable suppression bandwidth was limited by the carrier frequency constraints. Jian et al. [7] developed a dynamic harmonic torque cancelation method to reduce cogging torque. Zhang et al. [8] proposed a finite control set model predictive control strategy that dynamically adjusts the d–q axis current references to compensate for low-order air gap magnetic-field harmonics, achieving improved vibration suppression over a wide speed range compared with conventional PI control. Additionally, Hwang et al. [9] proposed a zero-sequence voltage compensation strategy for dual-three-phase PMSMs to suppress common-mode voltage and associated vibration. Chen et al. [10] employed a sliding-mode observer to estimate magnetic saturation and harmonic currents, followed by feedforward compensation to reduce low-frequency electromagnetic force fluctuations. However, the dynamic performance was limited by the convergence speed of the observer.

Structural optimization has been demonstrated as an effective approach for suppressing electromagnetic vibration and noise in PMSMs. Recent studies have systematically explored various structural optimization strategies, including pole–slot combination optimization [11–15], stator–rotor topology optimization [16–18], rotor skewing [19–22], and stator skewing slot [23–25], providing a theoretical foundation for low-noise PMSM design. Wang et al. [11] compared various fractional-slot surface-mounted permanent magnet motors and found that the 18-slot/10-pole configuration effectively suppressed torque ripple while eliminating unbalanced magnetic forces. Pedram et al. [12] investigated the influence of pole pair numbers on vibroacoustic performance using the multi-slice subdomain method. Zhang et al. [16] demonstrated that rotor auxiliary slots can suppress electromagnetic harmonics by optimizing air gap flux distribution. Shen et al. [18] reduced electromagnetic force harmonics by integrating stator auxiliary slots with rotor magnetic barriers and optimizing slot depth and barrier inclination angle. Zhu et al. [19] demonstrated that coordinated optimization of rotor skew angle and permanent magnet geometry can effectively suppress harmonic components in PMSM air gap magnetic fields. Jang et al. [21] developed a novel skewing method for railway traction motors and verified its effectiveness under high-voltage operating conditions. Sun et al. [23] reduced electromagnetic force fluctuations in moving-magnet-type linear synchronous motors through an independent coil structure design.

Although control algorithms can effectively attenuate motor vibration, their practical implementation in vehicular motor controllers may be constrained by hardware resources, computational burden, and limited control bandwidth. Therefore, motor design optimization has emerged as a fundamental approach for reducing electromagnetic vibration at the source. Existing rotor-related optimization studies mainly focus on stator slot skewing, rotor skewing, and pole–slot combination optimization. However, stator slot skewing and rotor skewing may degrade PMSM performance and increase manufacturing complexity. Moreover, pole–slot combinations are usually determined during the initial electromagnetic design stage.

In recent years, additional structural optimization approaches, including asymmetric magnet arrangements, segmented rotors, rotor offset techniques, and non-uniform air gap designs, have been investigated for electromagnetic vibration and cogging torque reduction. Although these methods have achieved certain vibration reduction effects, they often require substantial modifications to rotor topology, introduce additional manufacturing complexity, or consider only a limited number of structural parameters. Furthermore, most existing studies investigate individual structural features or limited parameter combinations, whereas the coupled effects of multiple asymmetric rotor parameters on electromagnetic vibration remain insufficiently explored. Table 1 summarizes representative structural optimization methods for PMSM vibration reduction and highlights their differences from the proposed approach. As shown in Table 1, existing structural optimization methods primarily investigate individual structural modifications or limited combinations of design variables. In contrast, the proposed method performs coordinated optimization of multiple asymmetric rotor parameters, including permanent magnet geometry, magnet position, and auxiliary slot dimensions, through a sensitivity-analysis-assisted surrogate-based optimization framework.

Table 1. Comparison of representative structural optimization methods for PMSM vibration reduction.

Literature	Structural Method	Design Variables	Optimization Method	Main Improvement	Limitation
Zhu et al. [19]	Rotor skew	Skew angle	Parametric optimization	Reduced electromagnetic force harmonics	Increased manufacturing complexity
Ge et al. [20]	Step-skew rotor	Skew step and angle	FEM optimization	Cogging torque reduction	3D manufacturing required
Shen et al. [18]	Auxiliary slots + magnetic barrier	Slot depth, barrier angle	Multi-parameter optimization	Reduced electromagnetic vibration	Rotor topology modified
Zhang et al. [16]	Non-uniform air gap	Air gap geometry	Multi-objective optimization	Noise and vibration reduction	Complex magnetic circuit
Peng et al. [22]	Segmented rotor	Segment number and arrangement	Comparative FEM analysis	Electromagnetic vibration mitigation	Increased assembly complexity
This work	Parameterized asymmetric rotor	PM width, thickness, offset and auxiliary slots (16 variables)	Sensitivity analysis + MOP + GA	Cogging torque ↓82.8%; torque ripple ↓17.9%; 48th EM force ↓50.7%; vibration ↓2.5 dB	No rotor skew or segmented magnets required

To mitigate PMSM vibration, this paper proposes an asymmetric rotor structure. An electromagnetic analytical model and a finite element model are developed for an eight-pole 48-slot interior permanent magnet synchronous motor. Addressing the prototype's excessive cogging torque and prominent 48th-order vibration response, we optimized the asymmetric rotor parameters using the Metamodel of Optimal Prognosis (MOP) coupled with genetic algorithms. Simulation results validate both the optimization methodology and the enhanced motor structure's effectiveness.

2. Modeling and Characteristics Analysis for PMSM

Modern vehicular PMSMs feature high rotational speeds, high power density, and lightweight structures, which introduce increased challenges in electromagnetic vibration suppression. This section establishes the electromagnetic field model and vibration response analysis model of the PMSM using finite element analysis. Subsequently, simulation-based vibration analysis is performed to investigate the electromagnetic excitation characteristics and vibration response of the motor.

2.1. PMSM Model

The investigated motor is an eight-pole 48-slot interior permanent magnet synchronous motor (IPMSM) designed for electric vehicle applications. It adopts a double-layer V-type rotor configuration, with the corresponding structural parameters listed in Table 2, and an eight-layer flat-wire stator winding. The material properties of the main motor components are summarized in Table 3.

Table 2. Design parameters for vehicular PMSM.

Parameter	Value	Unit
The inner/outer diameter of the stator	150.4/220	mm
The inner/outer diameter of the rotor	53/147.65	mm
Length of the stator	130	mm
Angle of the permanent magnet	90/110	°
Width of the permanent magnet	19.5/9	mm
Thickness of the permanent magnet	5.54/3.7	mm
Pole number	8	-
Slot number	48	-

Table 3. Constituent materials for individual motor components.

Component	Material	Density (kg/m^3)	Modulus of Elasticity (MPa)	Poisson's Ratio
Stator	35SW1900	9768	185,000	0.3
Rotor	35SW1900	9768	185,000	0.3
Magnet	N48UH	7300	150,000	0.3
Winding	Copper	8933	94,681	0.29
Shell	ADC12	2900	69,000	0.33
Reducer	ADC12	2900	69,000	0.33
Controller	ADC12	2900	69,000	0.33

In finite element analysis (FEA), mesh quality plays a critical role in determining simulation accuracy. Although a finer mesh improves numerical accuracy, it substantially increases computational cost. Therefore, an appropriate trade-off between accuracy and computational efficiency is required in electromagnetic field simulations. The mesh density should be carefully selected based on the characteristics of the electromagnetic field and available computational resources. Considering the non-uniform electromagnetic field distribution within different motor regions, different meshing strategies are applied to individual components. Among these regions, the air gap mesh density has the greatest influence on the accuracy of air gap flux density, cogging torque, and electromagnetic torque ripple calculations. Therefore, a refined mesh is adopted in the air gap region. The air gap is radially divided into six mesh layers to accurately capture the air gap flux density distribution. A relatively fine mesh is also applied to the stator teeth to accurately capture local flux density variations. For other regions, adaptive mesh sizes are selected according to local electromagnetic field variations to maintain sufficient accuracy while reducing computational cost. The mesh parameters of different components are summarized in Table 4, and the final mesh distribution is presented in Figures 1 and 2.

Table 4. Mesh size of each region.

Area	Sizing Grid
Stator/rotor	5 mm
Air gap	0.5 mm
Winding	0.8 mm
Magnetic steel	1 mm

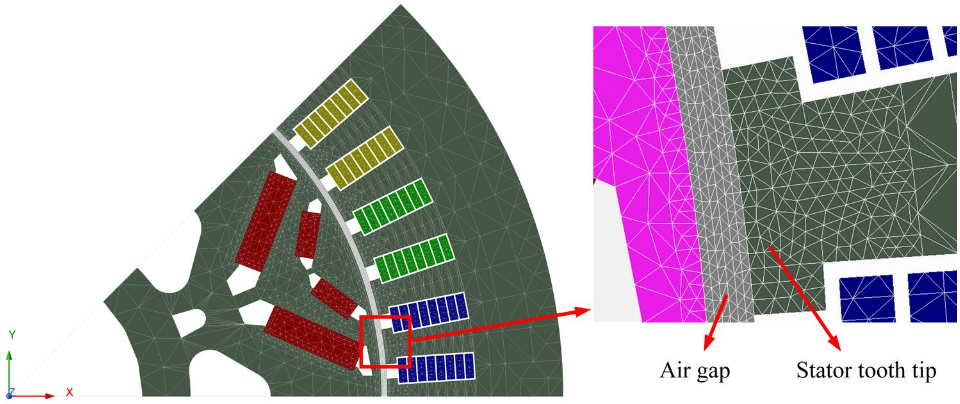

Figure 1. Meshing of the electromagnetic field model.

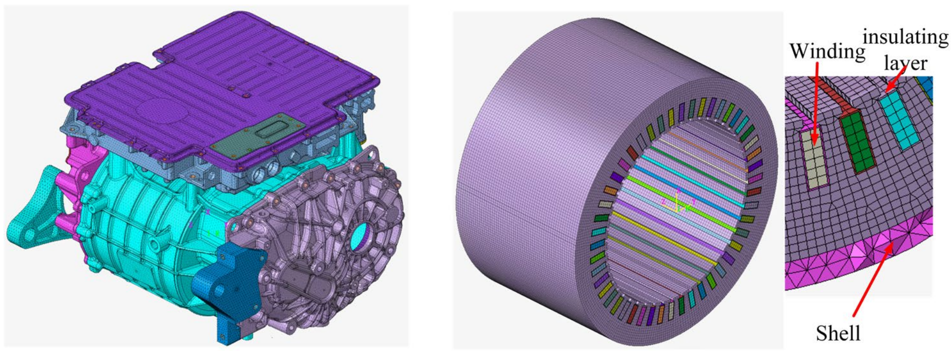

Figure 2. Three-dimensional finite element model of the electric drive assembly.

A refined finite element model of the electric drive assembly is developed using HyperMesh 2024. HyperMesh is used to generate high-quality meshes for each component of the electric drive assembly, considering both computational efficiency and simulation accuracy. During mesh generation, structural characteristics and load transfer paths are considered, and local mesh refinement is applied in critical regions to accurately capture the dynamic response of the electric drive assembly under vibration excitation. To accurately represent mechanical interactions and load transfer among internal components, a shared-node approach is adopted at critical connection regions. This approach ensures nodal continuity between adjacent structures and avoids numerical errors caused by node mismatch or discontinuous interfaces, thereby improving the reliability of the finite element analysis. After mesh generation, material properties are assigned to each component according to their actual material characteristics. The detailed material parameters are listed in Table 3.

It should be noted that the stator core is not a homogeneous solid structure but consists of numerous stacked silicon steel laminations. Due to the laminated structure, the stator core exhibits equivalent orthotropic mechanical behavior at the macroscopic scale, resulting in direction-dependent mechanical properties. Therefore, the stator core cannot be accurately represented as an isotropic material in the finite element model. Instead, equivalent mechanical properties, including Young's modulus, Poisson's ratio, and density, are defined based on the characteristics of the laminated structure to accurately characterize the dynamic response of the stator core under vibration excitation. The detailed material parameters are presented in Figure 3.

Name	Value	Table
⊟ **Common Properties**		
Density	9.768e-06 kg/mm3	
⊟ **Mechanical Properties**		
⊟ **Elastic**		
C11	380230 MPa	
C12	199220 MPa	
C22	289370 MPa	
C13	96272 MPa	
C23	54194 MPa	
C33	244010 MPa	
C44	168940 MPa	
C55	24059 MPa	
C66	24059 MPa	
Expansion_11		
Expansion_22		
Expansion_33		
Stiffness Matrix Vs Temperature		none

Figure 3. Material properties.

After assigning material properties to each component, the interface constraints between different components are defined. Specifically, tie constraints are applied between the stator core and insulation layer, windings and insulation layer, and stator core and housing. The remaining structural connections are modeled using RBE2 elements at bolt hole locations to represent rigid connections. The mounting positions of the electric drive assembly housing are constrained using bushing elements. After completion of the finite element model, free modal analysis is performed on the stator assembly. The first four modal shapes and corresponding natural frequencies are extracted, as shown in Figure 4. Different modal shapes exhibit distinct spatial distributions of nodes and antinodes. The closer the color is to red, the greater the amplitude of the vibration; conversely, the closer it is to blue, the lower the amplitude of the vibration. The simulation results indicate that the first natural frequency of the stator assembly is 5982 Hz.

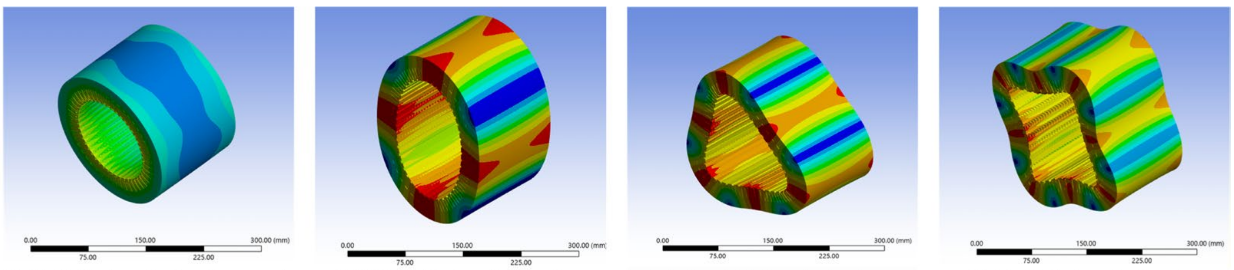

(a) (0, 0) Order of vibration mode, 5982Hz (b) (0, 2) Order of vibration mode,1567Hz (c) (0, 3) Order of vibration mode,4135Hz (d) (0, 4)Order of vibration mode,7354Hz

Figure 4. Stator mode shapes and modal frequencies.

2.2. Electromagnetic Characteristics Analysis for PMSM

Figure 5 presents the simulated no-load back electromotive force (BEMF) waveforms, which exhibit deviations from ideal sinusoidal characteristics and evident harmonic distortions in the three-phase induced voltages. Harmonic spectrum analysis identifies prominent 3rd, 5th, 7th, 9th, and 11th order harmonics in the BEMF.

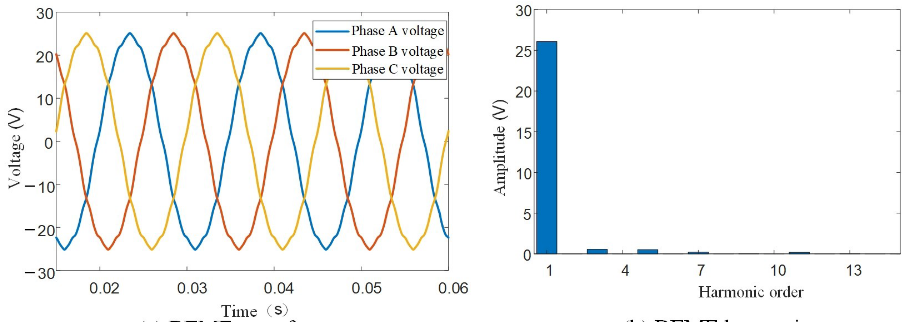

(a) BEMF waveform (b) BEMF harmonic

Figure 5. No-load BEMF and harmonic content.

The stator slotting effect introduces a non-uniform circumferential distribution of air gap permeance, which varies periodically with rotor position. As the rotor rotates, the periodic variation in air gap permeance causes changes in magnetic co-energy, thereby producing cogging torque, which can be expressed as follows:

$$T_{cog} = \frac{\partial W}{\partial \theta} \quad (1)$$

where W is the magnetic field energy, and θ is the rotor angle.

Equation (1) can be rewritten in Fourier series form as follows:

$$T_{\mathrm{cog}}(\alpha) = \frac{\pi z L_{\mathrm{Fe}}}{4\mu_0}(R_2^2 - R_1^2)\sum_{n=1}^{\infty} nG_n B_{rn} \sin(nz\alpha) \quad (2)$$

where z denotes the number of stator slots; L_{Fe} is the effective stack length; μ_0 is the permeability of free space; R_1 and R_2 are the inner and outer stator radii; G_n is the n-th Fourier coefficient of the air gap permeance; B_{rn} is the n-th Fourier coefficient of the squared magnet remanence; and n is the harmonic order.

Cogging torque induces output torque ripple, particularly at low speeds, resulting in motor vibration and consequent noise radiation. Figure 6 displays the no-load cogging torque profile at 1°/s rotational speed, revealing a 7.5° periodic variation with a peak-to-peak amplitude of 1.278 Nm.

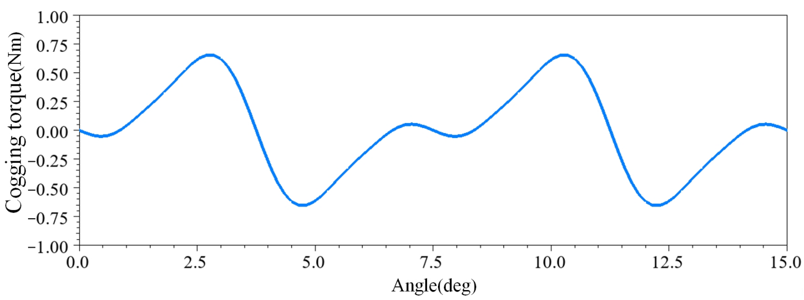

Figure 6. Cogging torque.

Figure 7 presents the circumferential distributions of the radial and tangential components of air gap magnetic flux density in the PMSM. The radial component exhibits distinct periodic variations that reflect the pole pair configuration, with each pole pair corresponding to one complete waveform cycle. The waveform consists of a nearly sinusoidal fundamental component superimposed with higher-order harmonic components, where cogging effects introduce waveform distortions. The harmonic spectrum reveals a fundamental amplitude of 0.86 T, accompanied by 3rd, 5th, 7th, 9th, 11th, and 13th harmonics, with the 5th harmonic demonstrating the highest magnitude.

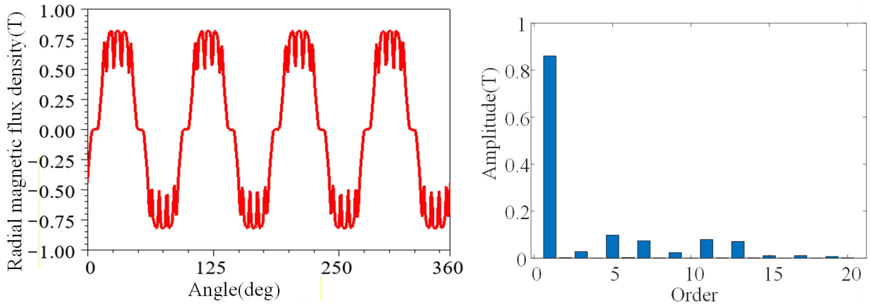

Figure 7. Magnetic density and harmonic content of radial air gap.

Figure 8 presents the output torque characteristics of the PMSM under an effective current of 520 A and a rotational speed of 1000 rpm. The simulation results show an average torque of 324.40 Nm and a peak-to-peak torque ripple of 17.02 Nm, corresponding to a torque ripple rate of 5.24%, calculated using Equation (3).

$$T_{Ripple} = \frac{T_{\max} - T_{\min}}{T_{avg}} \tag{3}$$

where $T_{\max}$ and $T_{\min}$ are the maximum and minimum values of the output torque, respectively, and T_{avg} is the average torque.

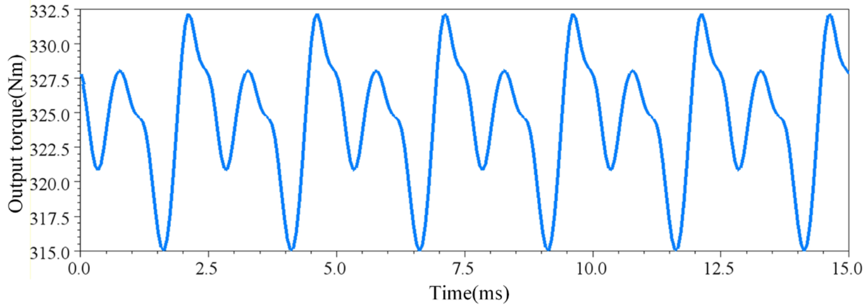

Figure 8. Motor output torque under steady-state conditions.

2.3. Vibration Characteristics Analysis for PMSM

Considering the slot–pole combination, slotting-related electromagnetic force harmonics are expected to be the dominant excitation sources of motor vibration [7,11,15]. For the investigated four-pole-pair, 48-slot PMSM, the fundamental slot harmonic corresponds to the 48th-order electromagnetic force component because the slot number determines the dominant spatial harmonic order. Therefore, the 24th, 48th, and 96th orders are selected for comparison to investigate the fundamental slot harmonic and its related components. Figure 9 presents the order-dependent vibration responses under external characteristic operating conditions. The 48th-order electromagnetic force produces the most significant vibration response, with a peak value of 109.7 dB at 7424 rpm. The 24th-order electromagnetic force generates noticeable vibration responses in the speed range of 14,000–16,000 rpm, whereas the 96th-order component exhibits a relatively smaller response peak near 3712 rpm. The acceleration responses are converted into decibel values using Equation (4) for quantitative comparison.

$$A_{dB} = 20\log\frac{a_{real}}{a_{ref}} \tag{4}$$

where A_{dB} is the acceleration level after decibel conversion, a_{real} is the actual value of acceleration, and a_{ref} is the acceleration reference value, 1 mm/s^2 is taken in this paper.

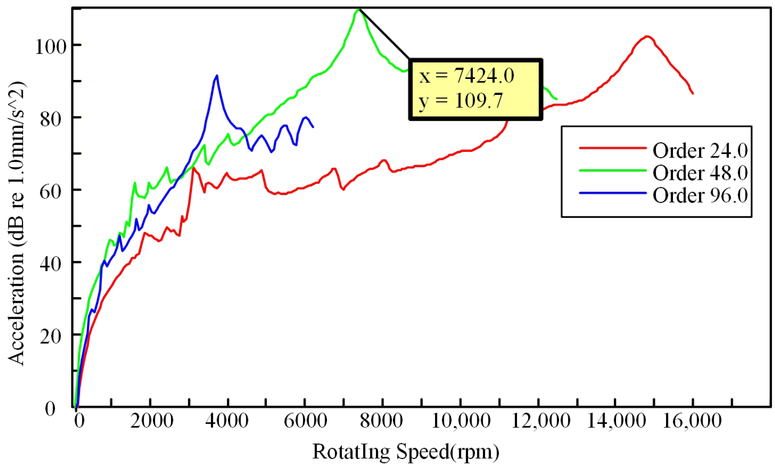

Figure 9. Order-dependent vibration responses under sinusoidal current excitation during motor external characteristic operation.

3. Experimental Validation

Model accuracy is essential for ensuring the reliability of the simulation results. To verify the effectiveness of the model and ensure that it can accurately reflect the actual dynamic characteristics of the PMSM, a test bench, as shown in Figure 10, is constructed for experimental validation. Both steady-state and transient experiments are conducted to evaluate the PMSM performance under different operating conditions, thereby verifying the consistency between the simulation results and experimental measurements.

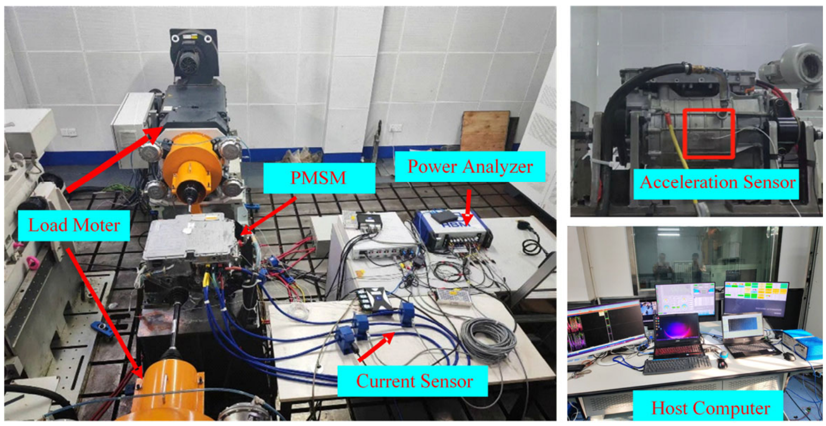

Figure 10. Experiment bench of PMSM.

A triaxial accelerometer is radially mounted on the motor housing to measure vibration responses. Low-impedance copper conductors are used to connect the three-phase windings to high-precision current sensors for accurate phase current acquisition. An HBM power analyzer synchronously records motor operating parameters, including vibration, current, voltage, speed, and torque, together with controller CAN signals.

Figure 11 presents the measured and simulated BEMF waveforms and harmonic spectra of the motor at 1000 rpm. The experimental (solid line) and simulated (dashed line) waveforms in Figure 11a show good consistency, with slight deviations observed near the peak regions. Figure 11b shows similar harmonic distributions between the simulated and experimental results, with only a 0.6% deviation in the fundamental component (26.04 V experimentally and 25.86 V numerically) while maintaining similar amplitudes for higher-order harmonic components.

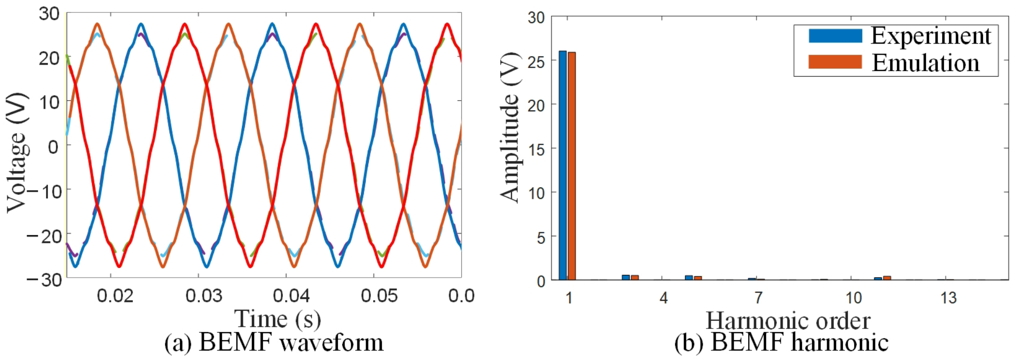

Figure 11. Motor BEMF waveform and harmonic amplitude.

Figure 12a compares the experimentally measured and simulated phase current waveforms under an operating condition of 1000 rpm and 200 Nm. It is observed that both the experimental and simulated waveforms exhibit noticeable distortion near the current peaks. Meanwhile, the time domain profiles of the measured and simulated currents show good consistency, indicating that the simulation model can effectively reproduce the motor operating characteristics under this condition. The corresponding frequency domain characteristics are further analyzed in Figure 12b, which illustrates the harmonic spectrum of the phase current. The amplitude distribution of different frequency components is clearly presented. For the low-order harmonic components, the experimentally measured amplitude of the 5th harmonic is 4.82 A, while the corresponding simulated value is 4.17 A. In the high-frequency region around the switching frequency, the maximum harmonic amplitudes obtained from experiments and simulations are 0.15 A and 0.17 A, respectively. These results indicate that the proposed simulation model can reproduce both the time domain characteristics and frequency domain behavior of the phase current with satisfactory accuracy.

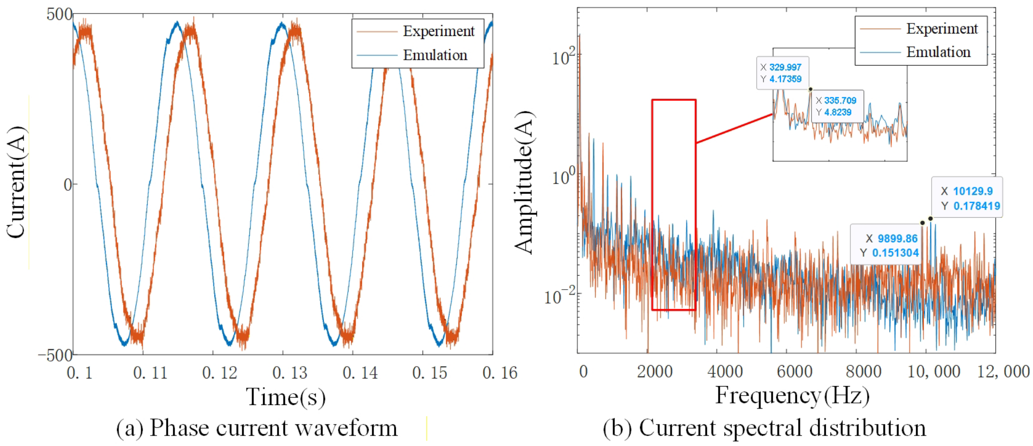

Figure 12. Phase current waveforms and spectral distribution of the motor (1000 rpm, 200 Nm).

Figure 13 compares the experimentally measured and simulated phase current waveforms under an operating condition of 2000 rpm and 200 Nm. It is observed that the measured and simulated waveforms exhibit good consistency in the time domain under this operating condition. In addition, the harmonic spectrum further indicates that the simulation model can effectively reproduce the frequency domain characteristics of the phase current.

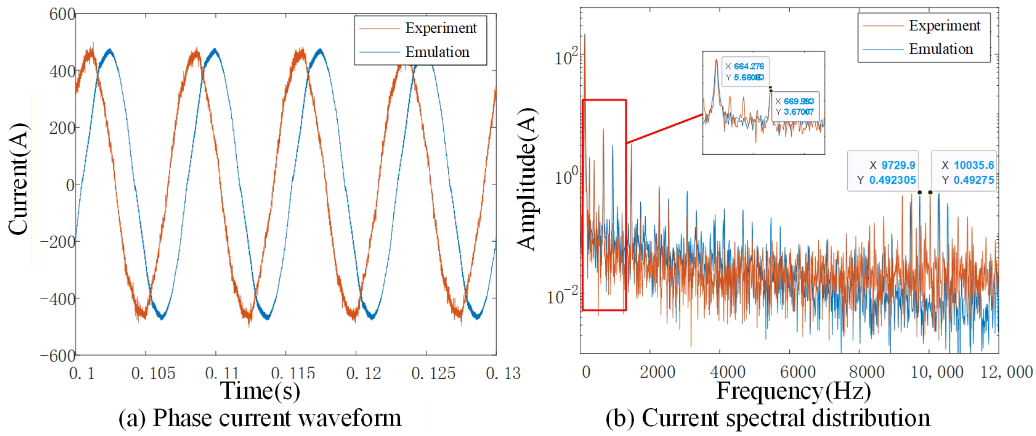

Figure 13. Phase current waveforms and spectral distribution of the motor (2000 rpm, 200 Nm).

Figure 14 presents the harmonic spectra of the phase voltage under different operating conditions. It is observed that the harmonic amplitudes remain generally consistent across different operating conditions. Under the condition of 1000 rpm and 200 Nm, the fifth-order harmonic amplitudes of the phase voltage obtained from simulation and experiment are 0.99 V and 0.90 V, respectively, while the maximum harmonic amplitudes around the switching frequency are 1.03 V and 1.27 V, respectively. Under the condition of 2000 rpm and 200 Nm, the fifth-order harmonic amplitudes obtained from simulation and experiment are 1.50 V and 1.04 V, respectively, and the maximum harmonic amplitudes around the switching frequency are 3.02 V and 3.39 V, respectively. These results indicate that the simulation model can effectively reproduce the phase voltage characteristics observed in the experiments.

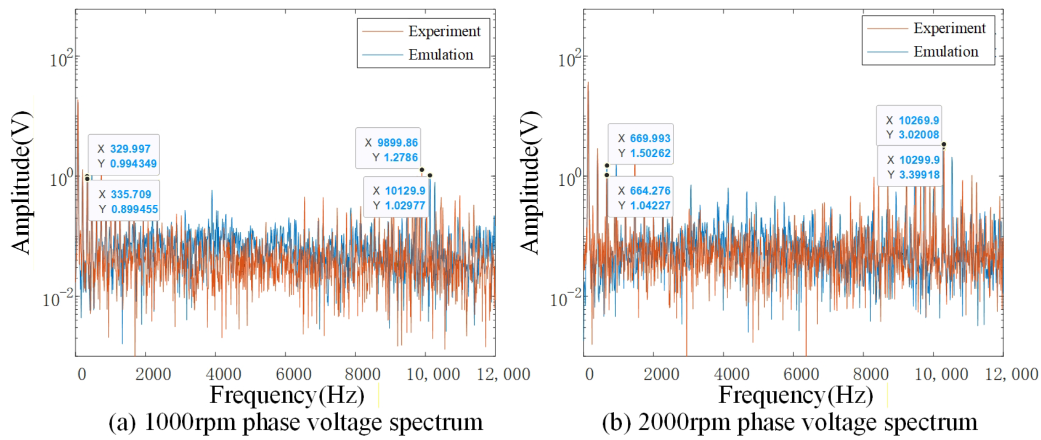

Figure 14. Phase voltage spectrum under different operating conditions.

Figure 15 presents the Campbell diagram of the radial vibration response measured at the monitoring point during maximum speed acceleration. As observed, the radial vibration spectrum exhibits distinct order characteristics, and the vibration components at different orders vary consistently with motor speed. With increasing motor speed, an apparent umbrella-shaped spectral structure emerges around the carrier frequency of 10 kHz, indicating high-frequency vibration components associated with inverter switching excitation. Moreover, these high-frequency components may interact with specific-order electromagnetic excitation frequencies within certain speed ranges, leading to locally amplified vibration responses.

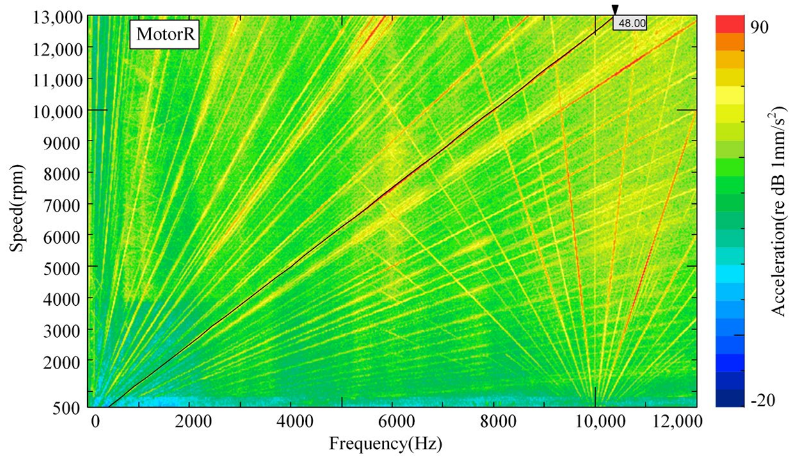

Figure 15. Vibration spectrum of the motor radial measurement point under external characteristic acceleration conditions.

During low-speed operation, the electromagnetic excitation frequencies are separated from the natural frequencies of the stator modes. Therefore, the resonance effect is limited, resulting in relatively low radial vibration amplitudes. As the speed increases, the excitation frequencies of different-order electromagnetic forces gradually approach the stator natural frequencies, causing the structural dynamic response to increase. When the electromagnetic excitation frequency approaches the zero-order modal frequency of the stator, the vibration response is significantly amplified, resulting in a pronounced increase in radial vibration amplitude. Particularly, a pronounced vibration peak is observed around 6000 Hz, where the 48th-order vibration component exhibits the strongest response. This indicates that the resonance between the 48th-order electromagnetic excitation and the stator structural mode is a dominant mechanism responsible for the vibration amplification under this operating condition.

Figure 16 presents the no-load BEMF waveform and 48th-order vibration response of the PMSM under the same operating conditions as those used in the simulation. The experimental and simulated vibration response curves exhibit consistent trends during the external characteristic acceleration process. Quantitative analysis reveals that the maximum vibration responses are 109.7 dB in simulation and 110.2 dB in experiments, corresponding to a deviation of only 0.45%.

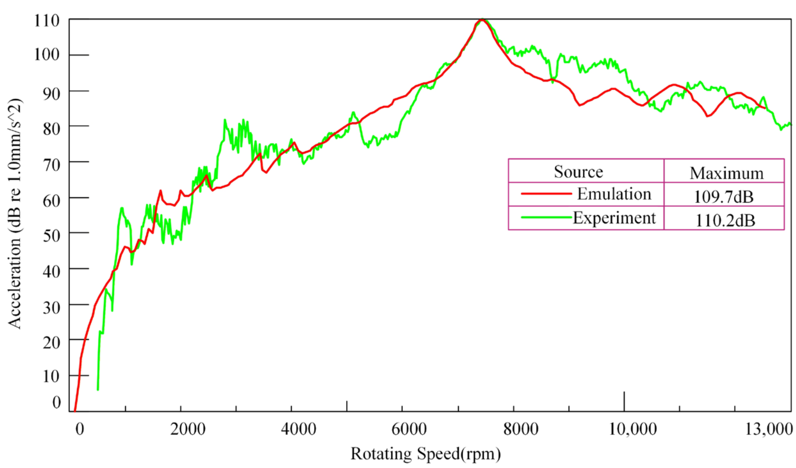

Figure 16. Comparison of radial 48th-order vibration simulation and experiment of motor.

In summary, the PMSM simulation model demonstrates good capability in predicting the electromagnetic and vibration characteristics under practical operating conditions, thereby providing a reliable basis for evaluating the effectiveness of the proposed structural optimization strategy.

4. Design and Optimization of Asymmetrical Rotor Structure for PMSM

To mitigate electromagnetic vibration and cogging torque in the PMSM, a parameterized asymmetric rotor structure is proposed. The degree of asymmetry is systematically determined by defining the permanent magnet geometry, magnet position, and auxiliary slot dimensions as design variables within predefined engineering constraints. A Design of Experiments (DOE)-based sensitivity analysis is first performed to identify the dominant design parameters, followed by the development of a MOP. Finally, a genetic algorithm is employed to determine the optimal asymmetric rotor configuration by minimizing cogging torque, torque ripple, and the 48th-order electromagnetic force while maintaining the required output torque.

4.1. Design of Asymmetrical Rotor Structure for PMSM

Figure 17 illustrates the key geometric parameters: (A, C, E, G) denote individual permanent magnet widths, (B, D, F, H) represent corresponding thicknesses, and (P1–P4) specify magnet positions within magnet slots, (W_1, W_2) for first/second layer magnet slots widths. The auxiliary slot dimensions comprise: (N_{w1}, N_{w2}) for D-axis auxiliary slot widths, and (N_{d1}, N_{d2}) for their respective depths.

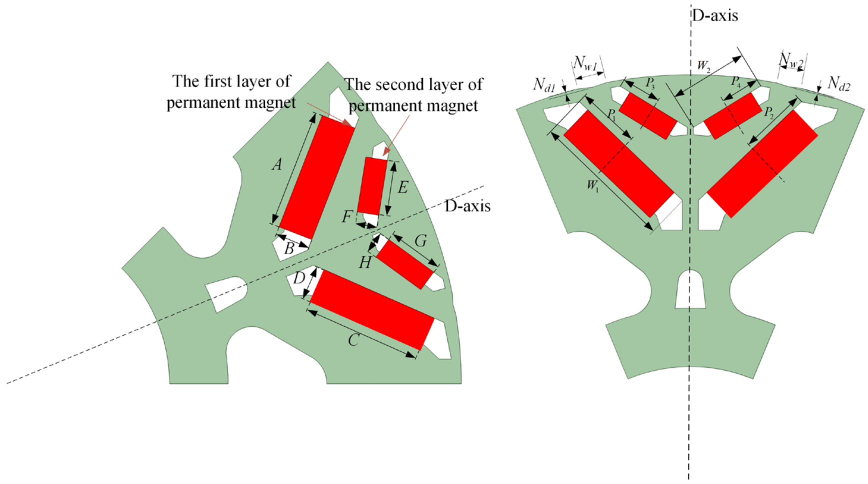

Figure 17. Schematic diagram of permanent magnet parameters.

The geometric parameters are defined as follows: first layer include permanent magnet width: W_{P1}; D-axis left–right width difference: W_{O1}; magnet thickness: T_{P1}; D-axis left–right thickness difference: T_{O1}; left/right magnet offsets: (S_{L1}, S_{R1}). Second layer include permanent magnet width: W_{P2}; D-axis left-right width difference: W_{O2}; magnet thickness: T_{P2}; D-axis left-right thickness difference: T_{O2}; left/right magnet offsets: (S_{L2}, S_{R2}). The parameter relationships in Figure 17 are as follows:

$$\begin{cases} A = W_{P1} + W_{O1} \\ C = W_{P1} - W_{O1} \\ B = T_{P1} + T_{O1} \\ D = T_{P1} - T_{O1} \\ P_1 = W_1/2 - S_{L1} \\ P_2 = W_1/2 - S_{R1} \end{cases} \quad \begin{cases} E = W_{P2} + W_{O2} \\ G = W_{P2} - W_{O2} \\ F = T_{P2} + T_{O2} \\ H = T_{P2} + T_{O2} \\ P_3 = W_2/2 - S_{L1} \\ P_4 = W_2/2 - S_{R1} \end{cases} \tag{5}$$

4.2. Sensitivity Analysis of Asymmetrical Rotor Structure Parameters for PMSM

This study focuses on four key performance metrics for PMSM optimization: cogging torque, torque ripple, output torque, and radial electromagnetic force. By establishing predetermined parameter ranges, this study systematically investigates their effects on motor performance, thereby improving the reliability of the sensitivity analysis. The parameter ranges of the motor model, determined based on design constraints and operating conditions are presented in Table 5.

Table 5. Optimization design variables with their feasible ranges.

Parameter	Initial Value (mm)	Value Range
T_{P1}	5.64	[4: 6]
T_{O1}	0	[−1: 1]
W_{P1}	19.4	[18: 20]
W_{O1}	0	[−2: 2]
S_{L1}	1.4	[−1.8: 1.8]
S_{R1}	1.4	[−1.8: 1.8]
T_{P2}	3.7	[3: 5]
T_{O2}	0	[−1: 1]
W_{P2}	9	[7: 9]
W_{O2}	0	[−2: 2]
S_{L2}	0	[−1.2: 1.2]
S_{R2}	0	[−1.2: 1.2]
N_{w1}	4	[2.5: 5]
N_{w2}	4	[2.5: 5]
N_{d1}	0	[0: 0.5]
N_{d2}	0	[0: 0.5]

The asymmetric rotor structure of the PMSM involves 16 design parameters during the optimization process. To improve design efficiency, sensitivity analysis is employed to quantify the effects of different parameters on motor performance and identify the most influential design variables. OptiSLang is an integrated optimization platform that provides functions including sensitivity analysis, design optimization, robustness evaluation, and reliability analysis. Owing to its graphical user interface and efficient model-building capability, OptiSLang facilitates the management of design parameters and objective functions, thereby improving the efficiency of the optimization process. The sensitivity analysis procedure implemented in OptiSLang generally consists of the following steps. After defining the input variables and response objectives, the design space is sampled using DOE or other appropriate sampling techniques. The responses of the sampled designs are subsequently calculated using the high-fidelity solver. Based on these samples, a surrogate model is constructed, and variance-based sensitivity indices are subsequently calculated from the surrogate model.

OptiSLang employs the MOP approach for sensitivity analysis. The MOP involves selecting the most appropriate surrogate model for a given set of input variables from candidate models, such as polynomial models with linear or quadratic bases and the least-squares moving approximation (MLS). In addition, the prediction accuracy of the response surface is quantitatively evaluated using a cross-validation-based method. Based on the obtained surrogate model, the CoP is calculated according to the MOP and response variance, and can be expressed as follows:

$$CoP = 1 - \frac{SS_E^{\text{Prediction}}}{SS_T} \tag{6}$$

$$S_T(X_a) = 1 - \frac{V(Y \mid X_a)}{V(Y)} \tag{7}$$

$$CoP(X_a) = CoP \cdot S_T^{MOP}(X_a) \tag{8}$$

where $SS_E^{\text{Prediction}}$ is the sum of squared prediction errors; $S_T^{MOP}(X_a)$ is the variance-based sensitivity factor under the optimal meta-model of prognosis; CoP is the overall predictive quality of the model; $CoP(X_a)$ represents the importance of parameter to the model.

The electromagnetic model of the PMSM established in the previous section was imported into OptiSLang for sensitivity analysis. Regarding the parameter settings, the maximum number of samples in OptiSLang was set to 300, ensuring sufficient design space coverage while maintaining computational efficiency. Meanwhile, the prediction coefficient was set to 0.9 as an important indicator for evaluating the goodness of fit of the surrogate model, ensuring high prediction accuracy. The influence factors of each parameter on motor performance were ranked in descending order, and the corresponding parameter influence maps are presented in Figures 18 and 19. The figures present the key parameters and their corresponding influence levels on multiple performance indicators, including cogging torque, torque ripple, output torque, the 24th-order electromagnetic force, and the 48th-order electromagnetic force.

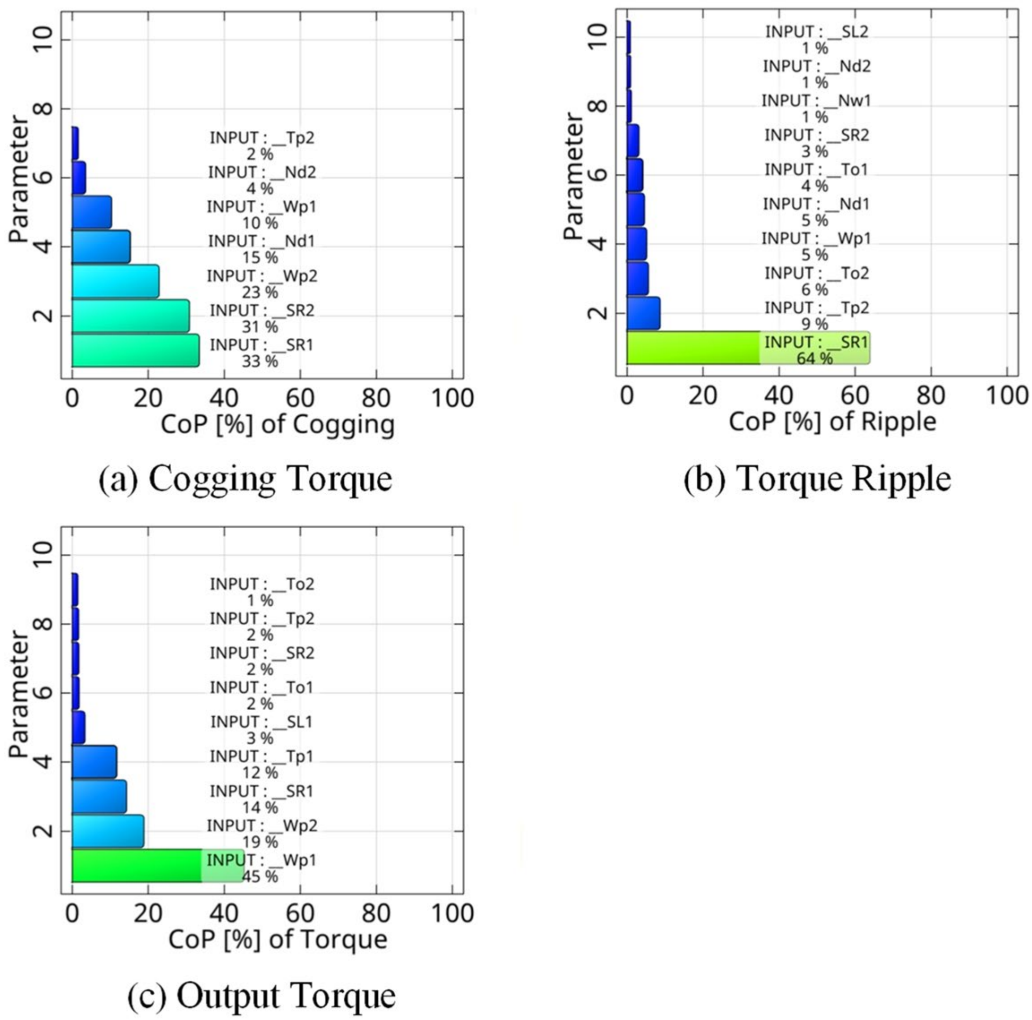

Figure 18. The main influencing factors of motor performance.

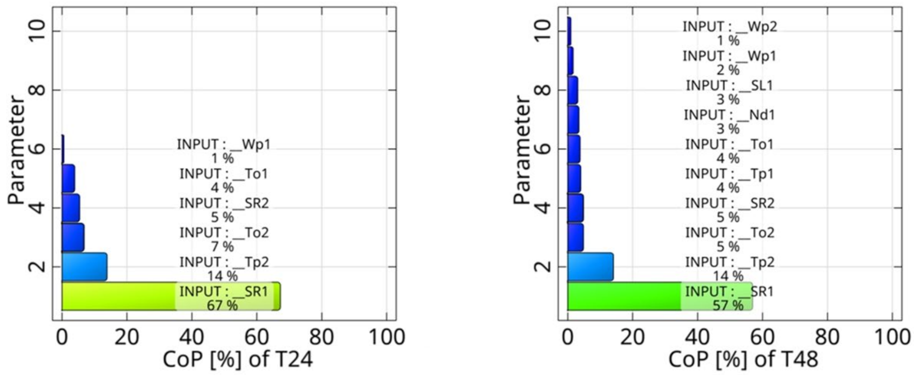

(a) 24th order electromagnetic force (b) 48th order electromagnetic force

Figure 19. The main influencing factors of electromagnetic force.

Figure 18 reveals significant influences on PMSM performance:

(1) Cogging torque: the dominant influencing parameters are the D-axis right-side permanent magnet offset, magnet width, and left-side auxiliary slot depth.
(2) Torque ripple: it is primarily influenced by the first-layer magnet parameters, which account for 64% of the importance in the MOP model.
(3) Output torque: strongly dependent on magnet width, thickness, and first-layer offset due to their direct impact on rotor magnetic field energy.

Figure 19 illustrates the sensitivity results of electromagnetic force components. The permanent magnet offset exhibits the most significant influence on the 24th- and 48th- order electromagnetic force components, with CoP values of 67% and 57%, respectively, followed by the second-layer magnet thickness. Other design parameters exhibit relatively limited influences on the investigated performance metrics.

Based on the sensitivity analysis results, which reveal the influence of different design parameters on PMSM performance, a high-fidelity surrogate model is constructed. The minimization of cogging torque, torque ripple, and the 48th-order electromagnetic force amplitude, together with the maintenance of output torque, are selected as the optimization objectives. A genetic algorithm is then employed based on the MOP surrogate model for global optimization. The genetic algorithm performs global searches in the multidimensional design space through selection, crossover, and mutation operations. Compared with existing studies that mainly optimize individual objectives such as cogging torque or torque ripple, the proposed objective functions simultaneously consider electromagnetic excitation and torque performance, thereby achieving a balance between vibration suppression and torque capability.

The multi-objective optimization function is defined as follows:

$$\min J = \left\{ T_{cog}, T_{Ripple}, A_{dB,48}, 1/T_{\max} \right\} \tag{9}$$

To obtain the final design solution from the multi-objective optimization results, weighting factors are introduced to evaluate the trade-off among different performance objectives, as expressed as follows:

$$F = \alpha_1 T_{cog} + \alpha_2 T_{Ripple} + \alpha_3 A_{dB,48} + \alpha_4 / T_{\max} \tag{10}$$

where α_1, α_2, α_3, and α_4 are the weighting factors of the four objectives, respectively, and all are set to 0.25.

To optimize the asymmetric rotor structure, the 16 parameters listed in Table 5 are selected as design variables for the optimization algorithm. The predefined ranges of these variables are also specified in Table 5.

During the optimization process, the population size, number of iterations, crossover probability, and mutation probability are set to 50, 100, 0.8, and 0.02, respectively. The Pareto-optimal solutions are obtained through iterative evolution of the genetic algorithm.

The optimized rotor parameters are presented in Table 6.

Table 6. Parameters of the rotor optimization scheme.

Parameter	Value (mm)
T_{P1}	5.47
T_{O1}	0.37
W_{P1}	19.4
W_{O1}	0
S_{L1}	0.18
S_{R1}	−0.94
T_{P2}	3.08
T_{O2}	−0.22
W_{P2}	9
W_{O2}	0
S_{L2}	0.76
S_{R2}	−0.49
Nw1	4.9
Nw2	4.5
Nd1	0.22
Nd2	0.20

5. Comparative Analysis of Motor Performance Before and After Optimization

Figure 20 compares the cogging torque characteristics of the PMSM before and after optimization. The original PMSM model exhibits a cogging torque amplitude of 1.278 Nm before optimization. After optimization, the cogging torque amplitude is reduced to 0.219 Nm, corresponding to an 82.81% reduction compared with the original design.

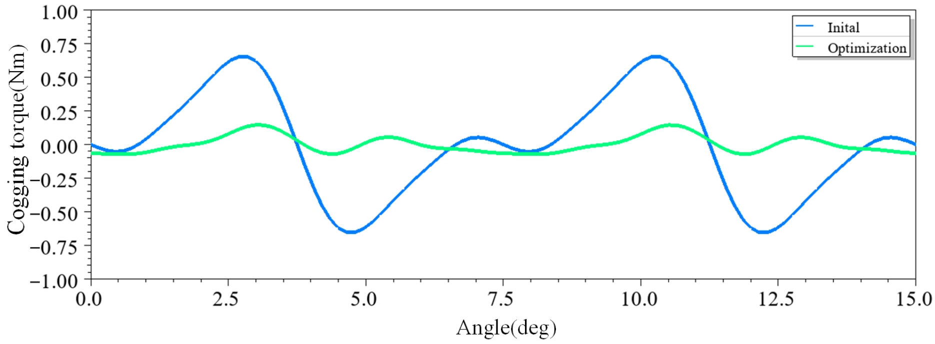

Figure 20. Comparison of cogging torque before and after optimization.

Figures 21 and 22 present the output torque characteristics and electromagnetic force spectra of the PMSM under an operating condition of 520 A effective current and 1000 rpm, comparing the performances before and after optimization. As shown in Figure 21, the average torque of the optimized motor decreases by 1.3%, from 324.40 Nm to 320.05 Nm, while the peak-to-peak torque ripple decreases by 17.9%, from 17.01 Nm to 13.97 Nm. The 48th-order electromagnetic force of the optimized model is well suppressed, from 2.60 N to 1.28 N, a decrease of 50.7% in Figure 22. However, the amplitudes of the 24th and 96th electromagnetic force components increase slightly after optimization.

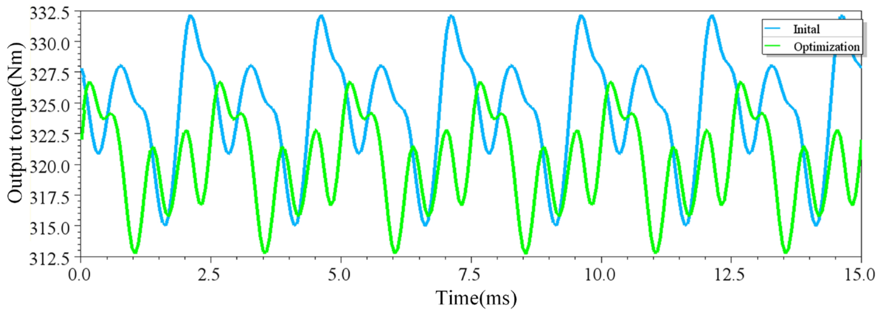

Figure 21. Comparative analysis of motor output torque profiles before and after optimization.

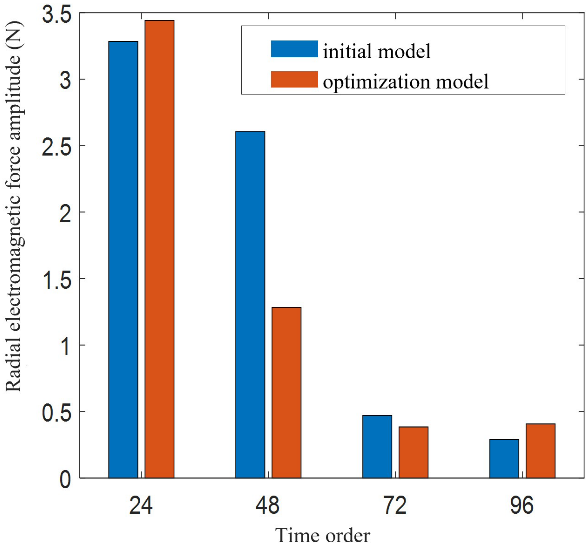

Figure 22. Spatial order 0 electromagnetic force.

Figure 23 presents the order-dependent vibration response characteristics of the optimized PMSM under external characteristic conditions. The 48th-order vibration component at the radial measurement point is reduced by 2.5 dB, from 109.7 dB to 107.2 dB.

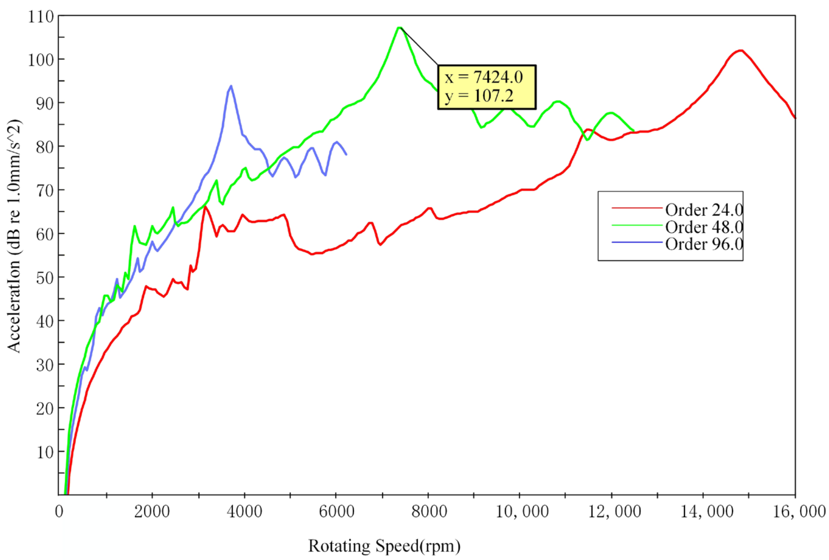

Figure 23. Optimizing the vibration response under the external characteristic conditions.

In summary, while maintaining the required output torque level, the proposed asymmetric rotor structure achieves significant reductions in cogging torque (82.8%), torque ripple (17.9%), and the 48th electromagnetic force component (50.7%). Compared with conventional rotor skewing and segmented rotor methods, the proposed asymmetric rotor structure avoids the need for rotor skewing processes or additional segmented magnets. Instead, vibration suppression is achieved through the coordinated optimization of permanent magnet geometry and position, thereby reducing structural complexity while preserving torque capability. These results demonstrate the effectiveness of the proposed asymmetric rotor design for mitigating PMSM vibration.

6. Results

This paper proposes an optimized asymmetric rotor structure to reduce cogging torque, torque ripple, and electromagnetic vibration in automotive PMSMs. The obtained sensitivity ranking provides practical guidelines for low-vibration PMSM design. Permanent magnet offset should be prioritized for suppressing electromagnetic vibration, whereas magnet width and thickness should be carefully adjusted to preserve torque capability. Auxiliary slot dimensions mainly contribute to cogging torque reduction and can be optimized after determining the primary magnetic parameters. Based on comprehensive parameter sensitivity analysis, this paper established an MOP-based surrogate optimization framework to guide multi-objective optimization targeting cogging torque minimization (82.81% reduction), torque ripple reduction, and 48th-order electromagnetic force attenuation (50.7% reduction), while preserving the required output torque level (only 1.3% reduction). The genetic algorithm optimization reduced the vibration amplitude by 2.5 dB, demonstrating the effectiveness of the asymmetric rotor structure in mitigating electromagnetic vibration while preserving torque capability.

In future work, a prototype of the optimized motor will be manufactured and experimentally tested to evaluate the vibration suppression performance of the proposed structure under practical operating conditions. Meanwhile, based on the experimental results, the vibration generation mechanisms will be further investigated to reveal the coupling relationships among electromagnetic excitations, structural modes, and assembly deviations. In addition, considering engineering application requirements, the manufacturing feasibility, magnet assembly tolerances, rotor balancing issues, and cost implications of the proposed optimization scheme will be systematically investigated. These investigations will provide further insights into the engineering implementation of the proposed motor structure.

Author Contributions: Conceptualization, J.H. and X.W.; methodology, J.H. and X.W.; software, J.H. and X.W.; validation, X.W., X.Z. and Z.Y.; formal analysis, J.H.; investigation, X.W.; resources, J.H.; data curation, X.Z. and Z.Y.; writing—original draft preparation, X.W.; writing—review and editing, J.H., X.Z. and Z.Y.; visualization, X.W.; supervision, X.Z. and Z.Y.; project administration, J.H.; funding acquisition, J.H. All authors have read and agreed to the published version of the manuscript.

Funding: This research was funded by the National Natural Science Foundation of China, grant number 52172364.

Data Availability Statement: The data supporting the findings of this study are available from the corresponding author upon reasonable request (hujianjun@cqu.edu.cn).

Conflicts of Interest: The authors declare no conflicts of interest.

References

1. Deng, W.Z.; Zuo, S.G. Electromagnetic Vibration and Noise of the Permanent-Magnet Synchronous Motors for Electric Vehicles: An Overview. *IEEE Trans. Transp. Electrif.* **2019**, *5*, 59–70. [CrossRef]
2. Wu, B.; Qiao, M.Z. A Review of the Research Progress of Motor Vibration and Noise. *Int. Trans. Electr. Energy Syst.* **2022**, *2022*, 1–10. [CrossRef]

3. Harries, M.; Woerndle, A.; De Doncker, R.W. Low Vibrations and Improved NVH in Permanent Magnet Synchronous Machines Due to Injection of Flux-Linkage Harmonics. *IEEE J. Emerg. Sel. Top. Power Electron.* **2022**, *10*, 1649–1657. [CrossRef]
4. Kang, L.; Xia, J.K.; Su, H.; Li, Z.X.; Liu, S.Q. Online Control Strategy for Radial Vibration Suppression of PMSM by Multiharmonic Current Injection Method. *IEEE Trans. Ind. Electron.* **2022**, *69*, 8692–8704. [CrossRef]
5. Ji, Z.K.; Cheng, S.W.; Ren, Q.; Li, X.H.; Lv, Y.J.; Wang, D. The Effects and Mechanisms of Periodic-Carrier-Frequency PWM on Vibrations of Multiphase Permanent Magnet Synchronous Motors. *IEEE Trans. Power Electron.* **2023**, *38*, 8696–8706. [CrossRef]
6. Wang, G.L.; Xiao, D.X.; Zhao, N.N.; Zhang, X.G.; Wang, W.; Xu, D.G. Low-Frequency Pulse Voltage Injection Scheme-Based Sensorless Control of IPMSM Drives for Audible Noise Reduction. *IEEE Trans. Ind. Electron.* **2017**, *64*, 8415–8426. [CrossRef]
7. Gao, J.; Xiang, Z.M.; Dai, L.T.; Huang, S.D.; Ni, D.C.; Yao, C. Cogging Torque Dynamic Reduction Based on Harmonic Torque Counteract. *IEEE Trans. Magn.* **2022**, *58*, 8103405. [CrossRef]
8. Zhang, G.W.; Yamamoto, A. Position Self-Sensing for Electrostatic Motors Under Amplitude-Modulated AC Operation. *IEEE Trans. Ind. Electron.* **2024**, *71*, 6809–6818. [CrossRef]
9. Hwang, S.I.; Kim, J.M. Opposite Triangle Carrier with SVPWM for Common-Mode Voltage Reduction in Dual Three Phase Motor Drives. *Energies* **2021**, *14*, 282. [CrossRef]
10. Chen, S.H.; Zhao, Y.L.; Qiu, H.T.; Ren, X.J. High-Precision Rotor Position Correction Strategy for High-Speed Permanent Magnet Synchronous Motor Based on Resolver. *IEEE Trans. Power Electron.* **2020**, *35*, 9716–9726. [CrossRef]
11. Wang, K.; Zhu, Z.Q.; Ombach, G.; Koch, M.; Zhang, S.; Xu, J. Electromagnetic Performance of an 18-Slot/10-Pole Fractional-Slot Surface-Mounted Permanent-Magnet Machine. *IEEE Trans. Ind. Appl.* **2014**, *50*, 3685–3696. [CrossRef]
12. Asef, P.; Perpiñà, R.B.; Lapthorn, A.C. Optimal Pole Number for Magnetic Noise Reduction in Variable-Speed Permanent Magnet Synchronous Machines with Fractional-Slot Concentrated Windings. *IEEE Trans. Transp. Electrif.* **2019**, *5*, 126–134. [CrossRef]
13. El-Refaie, A.M. Fractional-Slot Concentrated-Windings Synchronous Permanent Magnet Machines: Opportunities and Challenges. *IEEE Trans. Ind. Electron.* **2010**, *57*, 107–121. [CrossRef]
14. Islam, M.S.; Mikail, R.; Kabir, M.A.; Husain, I. Torque Ripple and Radial Force Minimization of Fractional-Slot Permanent Magnet Machines Through Stator Harmonic Elimination. *IEEE Trans. Transp. Electrif.* **2022**, *8*, 1072–1084. [CrossRef]
15. Kim, J.H.; Park, S.H.; Ryu, J.Y.; Lim, M.S. Comparative Study of Vibration on 10-Pole 12-Slot and 14-Pole 12-Slot PMSM Considering Tooth Modulation Effect. *IEEE Trans. Ind. Electron.* **2023**, *70*, 4007–4017. [CrossRef]
16. Zhang, Y.G.; Yang, Y.B.; Gu, Z.Y.; Li, L.Z.; Ma, T.C. Multi-Objective Optimization for Noise Reduction of IPMSM Based on Non-Uniform Air Gap. *IEEE Access* **2024**, *12*, 48819–48829. [CrossRef]
17. Xing, Z.Z.; Wang, X.H.; Zhao, W.L. Optimization of Stator Slot Parameters for Electromagnetic Vibration Reduction of Permanent Magnet Synchronous Motors. *IEEE Trans. Transp. Electrif.* **2022**, *8*, 4337–4347. [CrossRef]
18. Shen, Q.P.; Cheng, J.; Guo, D.; Yang, T.H. Analysis and Suppression of Electromagnetic Vibration Noise of Fractional-Slot Concentrated-Windings Interior PMSMs. *IEEE Trans. Transp. Electrif.* **2024**, *10*, 5270–5281. [CrossRef]
19. Zhu, S.D.; Zhao, W.X.; Ji, J.H.; Liu, G.H.; Mao, Y.X.; Liu, T. Investigation of Bread-Loaf Magnet on Vibration Performance in FSCW PMSM Considering Force Modulation Effect. *IEEE Trans. Transp. Electrif.* **2021**, *7*, 1379–1389. [CrossRef]
20. Ge, X.; Zhu, Z.Q.; Kemp, G.; Moule, D.; Williams, C. Optimal Step-Skew Methods for Cogging Torque Reduction Accounting for Three-Dimensional Effect of Interior Permanent Magnet Machines. *IEEE Trans. Energy Convers.* **2017**, *32*, 222–232. [CrossRef]
21. Jang, H.; Kim, H.; Nam, D.W.; Kim, W.H.; Lee, J.; Jin, C. Investigation and Analysis of Novel Skewing in a 140 kW Traction Motor of Railway Cars That Accommodate Limited Inverter Switching Frequency and Totally Enclosed Cooling System. *IEEE Access* **2021**, *9*, 121405–121413. [CrossRef]
22. Peng, C.; Wang, D.H.; Wang, B.D.; Li, J.C.; Wang, C.Q.; Wang, X.H. Different Rotor Segmented Approaches for Electromagnetic Vibration and Acoustic Noise Mitigation in Permanent Magnet Drive Motor: A Comparative Study. *IEEE Trans. Ind. Electron.* **2024**, *71*, 1223–1233. [CrossRef]
23. Sun, Q.W.; Wang, M.Y.; Liu, M.H.; Zhang, C.M.; Li, L.Y. Thrust ripple suppression analysis of moving-magnet-type linear synchronous motor based on independent coil. *Precis. Eng. J. Int. Soc. Precis. Eng. Nanotechnol.* **2024**, *91*, 223–232. [CrossRef]
24. Wang, S.M.; Hong, J.F.; Sun, Y.G.; Cao, H.X. Effect Comparison of Zigzag Skew PM Pole and Straight Skew Slot for Vibration Mitigation of PM Brush DC Motors. *IEEE Trans. Ind. Electron.* **2020**, *67*, 4752–4761. [CrossRef]
25. Zhou, Y.C.; Wei, X.C.; Yan, L.; He, X.H. Hybrid Analytical-Numerical Electromagnetic Vibration Calculation Method for Surface-Inserted PMSMs With Skewed Slots. *IEEE Trans. Energy Convers.* **2024**, *39*, 2654–2663. [CrossRef]